



**HAL**  
open science

## Independent reaction times method in Geant4-DNA: Implementation and performance

Jose Ramos-Mendez, Wook-geun Shin, Mathieu Karamitros, Jorge Domínguez-kondo, Ngoc Hoang Tran, Sébastien Incerti, Carmen Villagrasa, Yann Perrot, Václav Štěpán, Shogo Okada, et al.

### ► To cite this version:

Jose Ramos-Mendez, Wook-geun Shin, Mathieu Karamitros, Jorge Domínguez-kondo, Ngoc Hoang Tran, et al.. Independent reaction times method in Geant4-DNA: Implementation and performance. Medical Physics, 2020, 47 (11), pp.5919-5930. 10.1002/mp.14490 . hal-02988428v2

HAL Id: hal-02988428

<https://hal.science/hal-02988428v2>

Submitted on 17 Aug 2023

**HAL** is a multi-disciplinary open access archive for the deposit and dissemination of scientific research documents, whether they are published or not. The documents may come from teaching and research institutions in France or abroad, or from public or private research centers.

L'archive ouverte pluridisciplinaire **HAL**, est destinée au dépôt et à la diffusion de documents scientifiques de niveau recherche, publiés ou non, émanant des établissements d'enseignement et de recherche français ou étrangers, des laboratoires publics ou privés.



Distributed under a Creative Commons Attribution - NonCommercial - NoDerivatives 4.0 International License

# 1 Independent Reaction Times method in Geant4-DNA: implementation 2 and performance.

3 José Ramos-Méndez<sup>1)</sup> \*, Wook-Geun Shin<sup>2),3)</sup>, Mathieu Karamitros<sup>4)</sup>, Jorge Domínguez-Kondo<sup>5)</sup>, Ngoc  
4 Hoang Tran<sup>2)</sup>, Sebastien Incerti<sup>2)</sup>, Carmen Villagrasa<sup>6)</sup>, Yann Perrot<sup>6)</sup>, Václav Štěpán<sup>7)</sup>, Shogo Okada<sup>8)</sup>,  
5 Eduardo Moreno-Barbosa<sup>5)</sup> and Bruce Faddegon<sup>1)</sup>.

6 <sup>1)</sup> Department of Radiation Oncology, University of California San Francisco, San Francisco CA, 94115, USA.

7 <sup>2)</sup> Université de Bordeaux, CNRS/IN2P3, UMR5797, Centre d'Études Nucléaires de Bordeaux Gradignan,  
8 33175 Gradignan, France

9 <sup>3)</sup> Department of Radiation Convergence Engineering, Yonsei University, 26493 Wonju, Korea

10 <sup>4)</sup> Radiation Laboratory, University of Notre Dame, Notre Dame, In 46556, U.S.A.

11 <sup>5)</sup> Facultad de Ciencias Físico Matemáticas, Benemérita Universidad Autónoma de Puebla, Puebla PUE,  
12 72000 MEX.

13 <sup>6)</sup> IRSN, Institut de Radioprotection et de Sûreté Nucléaire, BP17, 92262 Fontenay-aux-Roses, France

14 <sup>7)</sup> Department of Radiation Dosimetry, Nuclear Physics Institute of the CAS, Prague, Czech Republic

15 <sup>8)</sup> KEK, 1-1, Oho, Tsukuba, Ibaraki 305-0801, Japan

16 \*Jose.RamosMendez@ucsf.edu

17

18 [Abstract.](#)

19 **Purpose:** The simulation of individual particle tracks and the chemical stage following water  
20 radiolysis in biological tissue is an effective means of improving our knowledge of the physico-  
21 chemical contribution to the biological effect of ionizing radiation. However, the step-by-step

22 simulation of the reaction kinetics of radiolytic species is the most time-consuming task in Monte  
23 Carlo track-structure simulations, with long simulation times that are an impediment to research.  
24 In this work, we present the implementation of the independent reaction times (IRT) method in  
25 Geant4-DNA Monte Carlo toolkit to improve the computational efficiency of calculating G-values,  
26 defined as the number of chemical species created or lost per 100 eV of deposited energy.

27 **Methods:** The computational efficiency of IRT, as implemented, is compared to that from  
28 available Geant4-DNA step-by-step simulations for electrons, protons and alpha particles  
29 covering a wide range of linear energy transfer (LET). The accuracy of both methods is verified  
30 using published measured data from fast electron irradiations for  $\cdot\text{OH}$  and  $e^-_{\text{aq}}$  for time-  
31 dependent G-values. For IRT, simulations in the presence of scavengers irradiated by cobalt-60  
32  $\gamma$ -ray and 2 MeV protons are compared with measured data for different scavenging capacities.  
33 In addition, a qualitative assessment comparing measured LET-dependent G-values with Geant4-  
34 DNA calculations in pure liquid water is presented.

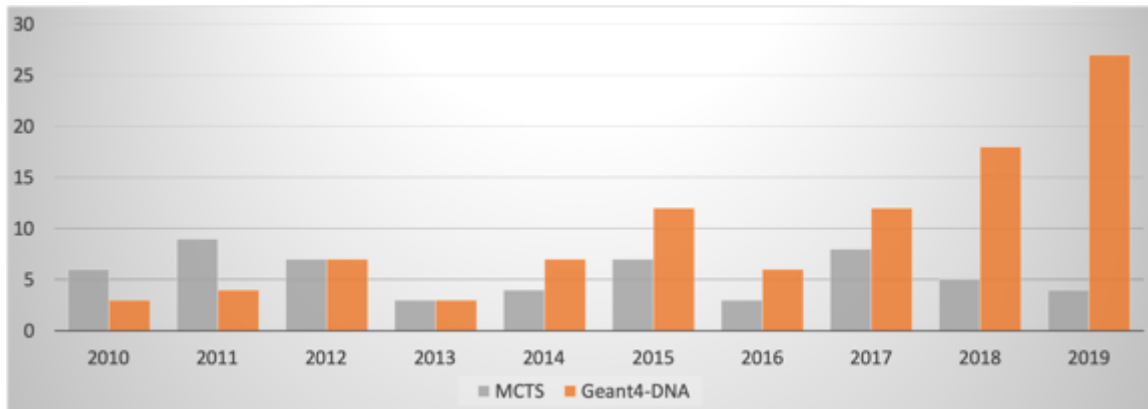
35 **Results:** The IRT improved the computational efficiency by three orders of magnitude relative to  
36 step-by-step while differences in G-values by 3.9% at 1  $\mu\text{s}$  were found. At 7 ps,  $\cdot\text{OH}$  and  $e^-_{\text{aq}}$  yields  
37 calculated with IRT differed from recent published measured data by  $5\% \pm 4\%$  and  $2\% \pm 4\%$ ,  
38 respectively. At 1  $\mu\text{s}$ , differences were  $9\% \pm 5\%$  and  $6\% \pm 7\%$  for  $\cdot\text{OH}$  and  $e^-_{\text{aq}}$ , respectively.  
39 Uncertainties are one standard deviation. Finally, G-values at different scavenging capacities and  
40 LET-dependent G-values reproduced the behavior of measurements for all radiation qualities.

41 **Conclusion:** The comprehensive validation of the Geant4-DNA capabilities to accurately simulate  
42 the chemistry following water radiolysis is an ongoing work. The implementation presented in  
43 this work is a necessary step to facilitate performing such a task.

44

45 [1 Introduction.](#)

46 Modeling the reaction kinetics of chemical species produced by radiolysis has important  
47 applications in radiobiology and medical physics. At the cellular level, this modeling complements  
48 the quantification of biological damage by accounting for the indirect contributions from the  
49 radiolytic species, extending the knowledge of the effects of ionizing radiation in biological tissue.  
50 Chemical reaction kinetics constitute a stochastic process that is in alignment with the  
51 capabilities of track-structure simulations using the Monte Carlo method. Together they  
52 encompass the physical and chemical processes of the interaction of ionizing radiation with  
53 biological tissue. Along the years, sophisticated Monte Carlo track-structure (MCTS) codes have  
54 been developed, including KURBUC <sup>1</sup>, PARTRACK <sup>2</sup>, RITRACKS <sup>3</sup>, TRAX-chem <sup>4</sup>, IONLYS-IRT <sup>5</sup>, and  
55 Geant4-DNA <sup>6-9</sup>. In some cases, the codes have the capability to integrate geometry models, like  
56 DNA in the cell nucleus, allowing the sampling of clustered DNA strand-breaks, which are the  
57 input of DNA repair models <sup>1,10-14</sup>. Until recently, MCTS codes have been restricted to the  
58 laboratories where they were developed, and then, their use in biology or medical physics fields  
59 have been limited, averaging only a few publications annually, as shown in Figure 1.



60

61 *Figure 1 : Number of publications per year in biomedical science listed in PubMed. Search parameters: Geant4-DNA or Monte*  
 62 *Carlo track-structure. Search criteria: appeared in the abstract of publications. Search date: February 10, 2020.*

63

64 More than 10 years have passed since the Geant4 Collaboration<sup>15–17</sup> released Geant4-DNA, today  
 65 the first open-source and multithreaded MCTS code<sup>6–9</sup>. Since 2013, this open source toolkit  
 66 provides models and tools to simulate the water radiolysis process, including the physical, pre-  
 67 chemical, and chemical stages<sup>18–20</sup>. Geant4-DNA is under active development (e.g.,<sup>9</sup>). This work  
 68 is being done in parallel with the development of TOPAS-nBio, a wrapper to the toolkit to  
 69 facilitate track structure and chemistry simulation of complex geometries incorporating cell  
 70 structures, including DNA<sup>21</sup>. The impact of Geant4-DNA in the medical physics field since its  
 71 introduction continues to increase (Figure 1). The development of Geant4-DNA is an ongoing  
 72 work that includes further refinement and validation of physical models, radiation chemistry  
 73 models, geometry models, damage scoring algorithms and computational efficiency  
 74 improvement methods.

75 It is well known that MCTS codes demand a high computational cost. The overload is intrinsic due  
 76 to the calculation of each and every ionization along the track of charged particles through

77 matter. In addition, the use of the step-by-step method (SBS) for the realization of chemical  
78 reactions between radiolysis products increases dramatically the computing time for the  
79 simulation of biological effects (>99% of the execution time for an alpha particle of 4 MeV/u  
80 simulated with Geant4-DNA). To mitigate this overload, at the physical stage the use of variance  
81 reduction techniques<sup>22</sup> and the combination of condensed-history and track-structure transport  
82<sup>23</sup> have shown significant enhancement of the computational efficiency of Geant4-DNA  
83 applications. For the chemical stage, the independent reaction times (IRT) technique has been  
84 developed to reduce the computational burden of simulating the reaction kinetics of chemical  
85 species<sup>24–26</sup>. IRT has been implemented in several MCST codes, mainly for the calculation of time-  
86 dependent radiolytic yields<sup>3,5,21,26–28</sup>. Given its flexibility, the algorithm can also accommodate  
87 the reaction of DNA molecules with reactive chemical species which leads to the estimation of  
88 early DNA damage, as shown in plasmid models<sup>29</sup> or the cell nucleus<sup>12</sup>. The high efficiency of IRT  
89 relative to step-by-step, and its flexibility to simulate biological damage, make this method a  
90 powerful tool with potential benefits to the research community. However, the availability of IRT,  
91 like open source MCTS, has been limited. For these reasons, the Geant4 collaboration has started  
92 to work actively on the implementation of this method in the code, either in its  
93 original/traditional version, using synchronous algorithm adapted to the calculation of DNA  
94 damage (Tran et al, submitted to Medical Physics), and an extended version that considers  
95 behavior of chemical species at boundaries<sup>30</sup>. A collective effort is also performed for comparing  
96 all these variants in order to specify the limits and advantages of each of them, which strongly  
97 depend on the applications.

98 In this work, we present details of the implementation and characterization of the IRT method in  
99 Geant4-DNA. We report the computational efficiency compared to SBS simulations and accuracy  
100 compared to experimental radiolytic yields. The implementation will be publicly released in  
101 forthcoming Geant4 version 10.7 Beta.

102

## 103 [2 Methods.](#)

### 104 [2.1 The Independent Reaction Times.](#)

105 The IRT method was developed to simulate reaction times in the diffusion kinetics process, as  
106 part of the simulation of the diffusion and reaction of radiolytic species and their reactive  
107 products following water radiolysis. The high computational efficiency of IRT compared to the  
108 alternative SBS method is achieved by avoiding the burden of simulating the detailed trajectory  
109 of each diffusing chemical species. In counterpart, this approach has the drawback of losing the  
110 spatial information of each individual chemical species. Instead, an iterative process is performed  
111 that begins at radiolysis and completes after all reactive species have reacted or an upper time  
112 limit has been reached. Following the independent pairs approximation, the initial positions of  
113 all the diffusive species produced at the end of the pre-chemical stage are used to simulate the  
114 reaction times between reactive pairs using probability functions. These functions represent  
115 solutions to the diffusion equation from the theory of diffusion kinetics. All the reactive pairs  
116 along with their reaction times are assembled into an array that is sorted out in an ascendant  
117 way according to reaction times. Subsequently, the realization of the reactions is performed by  
118 removing from the array each reactive pair, starting with the pair with the shortest reaction time,

119 and inserting the reactive products, if any. Each time a product is created, the corresponding  
120 reaction times with the remaining species in the array are sampled and resorted in an ascendant  
121 way. The process is finished when all the possible combinations are exhausted or an upper time  
122 limit is achieved, typically the  $10^{-7}$ - $10^{-6}$  s, signaling the end of the chemical stage, when the spatial  
123 distribution of species are considered as homogeneous<sup>31</sup>. Reactions with background solutions  
124 can be simulated as pseudo-first-order reactions with the continuum approach, assuming they  
125 are uniformly distributed in the background. In the continuum approach, each reactive species  
126 reacts with the background following an exponential distribution probability given by  $1 - \exp(-$   
127  $k[B] t)$ , where  $k[B]$  is the scavenging capacity of the solution<sup>26</sup>. For the implementation, the  
128 reaction times are obtained as  $t = -\log(U)/k[B]$ , where  $U$  is a random number uniformly  
129 distributed between 0 and 1.

### 130 *2.1.1 Reaction schemes.*

131 The implementation presented in this work, extends the previous scheme for SBS simulations of  
132 Geant4-DNA<sup>18,19</sup> developed on top of totally diffusion-controlled reactions (when two chemical  
133 species recombine with each other immediately at encounter), by incorporating the IRT method  
134 including partially diffusion-controlled reactions (when two chemical species do not recombine  
135 immediately when they encounter,<sup>32</sup>). The scheme to simulate the reaction times is based on  
136 the formalism developed<sup>25,33</sup>, and later presented elsewhere<sup>3,5,26</sup>. The reader is referred to these  
137 publications for the mathematical details. The main probability functions are summarized below.  
138 For totally diffusion-controlled reactions, the reaction times are sampled using the inverse of the  
139 probability functions solved for time  $t$ , given by Equations 1 and 2 for reactions where at least  
140 one chemical specie is neutral, and between charged particles, respectively.



141 
$$P_I(t | r_0) = \frac{\sigma}{r_0} \operatorname{Erfc} \left( \frac{r_0 - \sigma}{\sqrt{4Dt}} \right) \quad (1)$$

142 and,

143 
$$P_{III}(t | r_0) = \frac{\sigma_{\text{eff}}}{r_{\text{eff}}} \operatorname{Erfc} \left( \frac{r_{\text{eff}} - \sigma_{\text{eff}}}{\sqrt{4Dt}} \right) \quad (2)$$

144 where  $r_0$  is the initial separation between chemical species,  $\sigma$  is the reaction radius and  $D$  is the  
 145 sum of the diffusion coefficients. For charged particles,  $r_{\text{eff}}$  and  $\sigma_{\text{eff}}$  are the effective separation  
 146 distance and effective reaction radius, respectively. These values are scaled from the natural  
 147 separation and reaction radius to consider a Coulomb potential and are related by the Onsager's  
 148 radius  $r_c$  as follows

149 
$$r_{\text{eff}} = \frac{-r_c}{1 - \exp(r_c/r_0)}, \quad \text{and} \quad \sigma_{\text{eff}} = \frac{-r_c}{1 - \exp(r_c/\sigma)} \quad (3)$$

150

151 For partially diffusion-controlled reactions, the probability functions are assigned to a random  
 152 number  $U$  uniformly distributed between 0 and 1 (i.e.  $P_{II}(r, t | r_0) = U$ ) and solved numerically to  
 153 obtain the time,  $t$ . Equation 4 corresponds to reactions where at least one chemical species is  
 154 neutral, rewritten in terms of the diffusion  $k_{\text{diff}}$  and activation  $k_{\text{act}}$  reaction rate coefficients for  
 155 computational implementation.

156 
$$P_{II}(t | r_0) = \frac{k_{\text{act}}}{k_{\text{diff}} r_0 \alpha} \left[ \operatorname{Erfc} \left( \frac{r_0 - \sigma}{\sqrt{4Dt}} \right) - W \left( \frac{r_0 - \sigma}{\sqrt{4Dt}}, -\alpha \sqrt{4Dt} \right) \right] \quad (4)$$

157

158 where,  $\alpha = -(k_{act} + 4\pi\sigma D)/(4\pi\sigma^2 D)$  with  $k_{act}$  the activation reaction rate coefficient and  
159  $W(x, y) = \exp(2xy + y^2) \text{Erfc}(x + y)$ . Equation 5 corresponds to reactions between charged  
160 particles, rewritten in terms of  $k_{diff}$  and the observed reaction rate coefficient  $k_{obs}$ :

161

$$162 \quad P_{IV}(t | r_0) = \frac{\sigma_{eff} k_{obs}}{r_{eff} k_{diff}} [\text{Erfc}(b) - W(b, a)] \quad (5)$$

163 where,

$$164 \quad a = \frac{4\sigma^2 \alpha'}{r_c^2} \sqrt{\frac{t}{D}} \sinh^2\left(\frac{r_c}{2\sigma}\right), \quad \text{and} \quad b = \frac{r_c}{4\sqrt{Dt}} \left[ \coth\left(\frac{r_c}{2r}\right) - \coth\left(\frac{r_c}{2\sigma}\right) \right] \quad (6)$$

165 with  $\alpha'$  given by,

$$166 \quad \alpha' = \frac{k_{act}}{4\pi\sigma^2} + \frac{r_c D}{\sigma^2 (1 - \exp(-r_c/\sigma))} \quad (7)$$

167

### 168 *2.1.2 Implementation in Geant4-DNA.*

169 Geant4-DNA, an extension of the Geant4 toolkit, is an object-oriented simulation toolkit written  
170 in C++ for the simulation of the passage of particles through the matter, the subsequent radiolysis  
171 and the reaction kinetics of chemical species. The software provides the tools distributed in C++  
172 classes<sup>a</sup> which include functionalities to build geometry models, specify particle sources, invoke  
173 physics process and chemistry process, scoring capabilities, etc. In this way, Geant4-DNA allows  
174 building sophisticated simulations for radiobiology research. Details of the architecture of Geant4

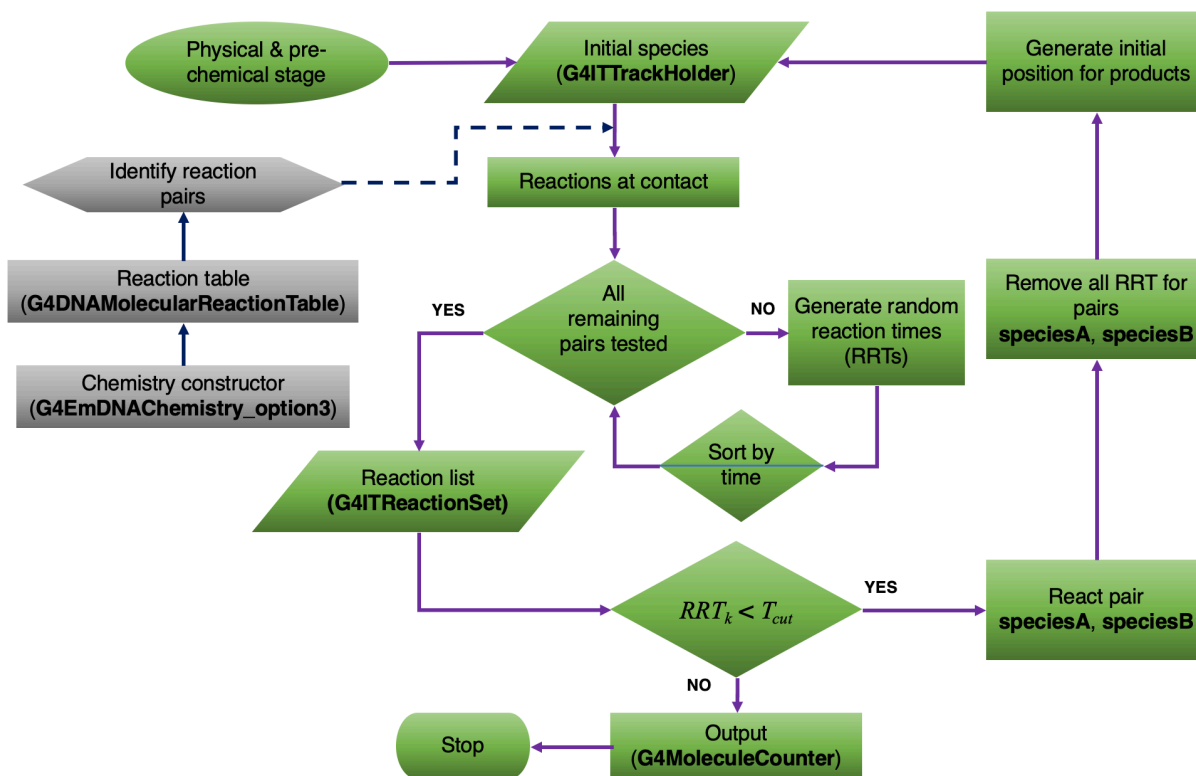
---

<sup>a</sup> A C++ class is a user-defined concrete representation of a concept (i.e. a type), designed to provide a new type that has no direct counterpart among the built-in C++ types.<sup>67</sup>

175 and Geant4-DNA can be found elsewhere <sup>6-9,17-20,34</sup>. Details of the implementation of IRT in  
 176 Geant4-DNA are presented here.

177

178



179

180 *Figure 2 : Flowchart of IRT implemented in Geant4-DNA (version 10.7 beta, June 2020). G4ITTrackHolder, G4ITReactionSet,*  
 181 *G4DNAMolecularReactionTable and G4MoleculeCounter classes are developments already available from the step-by-step*  
 182 *implementation* <sup>19, 35</sup>.

183 Figure 2 shows the flowchart diagram of the implementation of IRT in Geant4-DNA developed in  
 184 this work (version 10.7 beta, June 2020). The dissociation channels of the pre-chemical stage  
 185 (Table 1) and the chemical reactions are declared and initialized in the chemistry class

186 constructor<sup>b</sup> **G4EmDNAChemistry\_option3**, which includes the list of molecular chemical  
 187 species, chemical reactions and their type. The set of reactions implemented are those listed for  
 188 the RITRACKS software elsewhere <sup>3</sup>, see appendix A. Provisions are made within the class  
 189 constructor to facilitate activating or deactivating individual reactions in Geant4-DNA  
 190 applications. Parameters for the chemical reactions are pre-calculated in the  
 191 **G4DNAMolecularReactionTable** class. By the end of pre-chemical stage, the initial chemical  
 192 species are automatically stored in a vector defined in the **G4ITTrackHolder** class. From this class,  
 193 a loop is performed to identify all possible reactive pairs from all the initial chemical species.  
 194 Subsequently, reactions at contact are evaluated using equation 8 <sup>3,5,36</sup> which overcomes the  
 195 cases when the interparticle distance is smaller than the effective reaction radius and hence the  
 196 IRT method cannot be used, for example in equation 1 the probability is greater than one if  $r_0 <$   
 197  $\sigma$ .

$$P_{\text{react}} = \frac{-\exp\left(-\frac{r_c}{\sigma + \varrho}\right)}{\exp\left(-\frac{r_c}{\sigma}\right) - \exp\left(-\frac{r_c}{\sigma + \varrho}\right) - \left(\frac{k_{\text{diff}}}{k_{\text{act}}}\right)\left(1 - \exp\left(-\frac{r_c}{\sigma}\right)\right)} \quad (8)$$

199 In equation 8,  $\varrho = 0.29$  nm, the approximate distance between neighboring water molecules;  
 200 and  $P_{\text{react}} = 1$  for totally diffusion-controlled reactions ( $k_{\text{act}} \rightarrow \infty$ ) as expected.

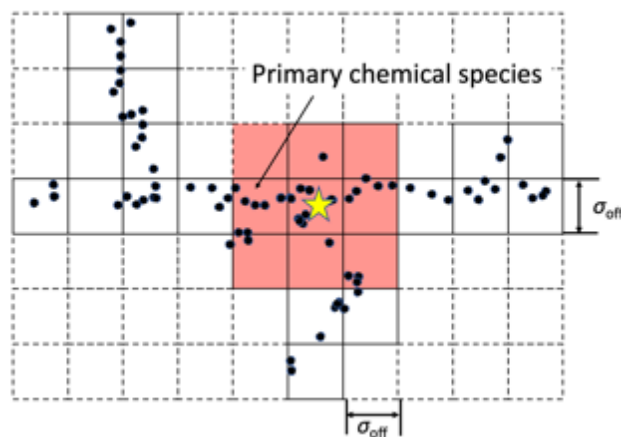
201 The identified remaining reactive pairs, defined internally as “reactions”, are stored in the  
 202 reaction list defined in the **G4ITReactionSet** class with their corresponding reaction time, called  
 203 random reaction time (RRT in figure 2). The RRT values are sampled depending on the type of  
 204 reaction using equations 1, 2, 4 and 5, whereas the adopted acceptance-rejection methods are

---

<sup>b</sup> A constructor is a function with the explicit purpose of initializing objects (i.e. construct) of a give type.<sup>67</sup>

205 described in detail elsewhere<sup>3</sup>. **G4ITReactionSet** uses an ordered multiset container to sort in  
206 ascending order the RRT values. Subsequently, one more loop is performed for the realization of  
207 reactions, that is, to remove from the reaction list the reactive pairs (named speciesA and  
208 speciesB in Figure 2), starting with the pairs having the shortest RRT value. All remaining  
209 “reactions” that include any of the reactive species involved are also removed. If chemical species  
210 are produced by the reaction, then all of the possible reactive pairs along with the remaining  
211 chemical species in **G4ITTrackHolder** are identified and inserted in the reaction list with the  
212 corresponding RRT value. The spatial positions of the products are calculated with the *position*  
213 *approach* described elsewhere<sup>24</sup>. Finally, the **G4MoleculeCounter** class counts the number of  
214 chemical species and calculates G-values (number of chemical species produced or lost per 100  
215 eV of deposit energy) as a function of time.

216



217

218 *Figure 3 : A schematic illustration of the voxelization of the chemical track into cubic voxels of side length  $\sigma_{off}$ . The black points*  
219 *represent chemical species at the end of the pre-chemical stage, the yellow star indicates a target molecule, and the red voxels*  
220 *represent scanned regions, searching for the target molecule.*

221 To reduce the computational burden of searching reactive pairs separated by long distances, we  
222 limit the search range for a reactive chemical species among its neighbors based on a confidence  
223 level for reaction. To this end, the simulation medium is voxelized into cubic voxels of side length  
224  $\sigma_{\text{off}}$  (Figure 3), the searching range described elsewhere<sup>19</sup>. The parameter  $\sigma_{\text{off}}$  was set to 550 nm,  
225 giving a 95% confidence level for the species with higher reaction rate ( $\text{H}_3\text{O}^+$ , table 2). Thus, for a  
226 given chemical species, shown with a yellow star in Figure 3, all the possible reactions are  
227 searched within the 27 voxels around it (in 3-dimensions).

228 To incorporate the IRT method within the chemistry framework of Geant4-DNA, new classes have  
229 been developed among the Geant4 kernel classes. In this way, the users can easily swap between  
230 the SBS method or the IRT method in any physics list (e.g. selecting **G4EmDNAChemistry\_option3**  
231 for IRT or **G4EmDNAChemistry up to option 2** for SBS), taking advantage of the features  
232 previously developed for the SBS method, described elsewhere<sup>18,19</sup>.

233

## 234 2.2 Verification.

### 235 *2.2.1 Physical models and water dissociation scheme.*

236 The simulation of the physical stage is done on a history-by-history basis, starting with a  
237 source particle traversing the geometry, ionizing atoms in its wake, followed by water radiolysis  
238 with diffusion and reaction of the reactive chemical species. For the simulation of physical  
239 interactions in liquid water (e.g. electronic excitation, ionization, elastic scattering, etc.), Geant4-  
240 DNA adopts a discrete approach (“track structure”) in which all interactions are explicitly  
241 simulated, without the use of cuts for the control of the production of secondary particles. Such  
242 an approach ensures a better accuracy, particularly adapted to low energy (< 100 eV) and small

243 dimension (< micrometer) particle tracking<sup>37</sup>. Geant4-DNA provides different sets of models for  
244 the simulation of physical interactions, assembled in “physics constructors” which assign each  
245 particle type to a list of physical interactions they can undergo along with the corresponding  
246 models needed to simulate such interaction. We previously described in detail the three  
247 alternative constructors currently available in Geant4-DNA, differing only by the theoretical  
248 approaches they adopt for the description of electron interactions and by their energy range  
249 coverage<sup>9</sup>

250         For this study, we selected the “G4EmDNAPhysics\_option2” physics constructor, which  
251 provides the largest energy coverage for electrons in Geant4-DNA (7.4 eV to 1 MeV). In brief, this  
252 constructor describes the interactions of electrons, photons, protons, neutral hydrogen, alpha  
253 particles and their charged states and heavier ions (<sup>7</sup>Li, <sup>9</sup>Be, <sup>11</sup>B, <sup>12</sup>C, <sup>14</sup>N, <sup>16</sup>O, <sup>28</sup>Si and <sup>56</sup>Fe).  
254 Regarding electron interactions, this constructor describes inelastic processes based on the  
255 formalism of the complex dielectric response function of liquid water, considering four ionization  
256 shells and five discrete electronic excitation states<sup>38</sup>. Ionization of the K-shell is calculated from  
257 the Binary-Encounter-Approximation-with-Exchange model<sup>39</sup>. Regarding the modeling of elastic  
258 scattering for electrons, for this work we have replaced the default model based on the partial  
259 wave theory by a newly developed model calculated using the ELSEPA code<sup>40,41</sup>. Regarding the  
260 thermalization distance of sub-excited electrons, the model adopted is derived from Monte Carlo  
261 simulations using cross-sections of Michaud et al<sup>42</sup> for amorphous ice, scaled by Meesungnoen  
262 et al<sup>43</sup> to consider the difference between amorphous and liquid-phase water. The model is  
263 applied with an upper energy limit of 7.4 eV. In the case of electrons induced by auto-ionization  
264 of excited water molecules at the pre-chemical stage, the thermalization distance is obtained as

265 if the electron has 1.7 eV of kinetic energy, based on empirical data. The effect of different  
266 thermalization models available in Geant4-DNA has been described elsewhere <sup>20</sup>.

267 The different parameters needed for the simulation of the physico-chemical and chemical  
268 stages of water radiolysis are gathered in a “chemistry constructor”, which contains all  
269 information available for simulation of the water molecule dissociation scheme, definition of  
270 molecular species (including charge, mass, diffusion constant and van der Waals radius) and  
271 chemical reactions they can undergo (including reaction rate coefficients). This constructor is  
272 named “G4EmDNAChemistry\_option3” and is designed exclusively for this IRT approach,  
273 opposed to the other chemistry constructors available in Geant4-DNA, which are only used for  
274 the SBS approach. The list of available constructors dedicated to the chemical stage simulation  
275 are summarized in the table 1. The dissociation scheme of water molecules, following physical  
276 ionizations or electronic excitations, and corresponding branching ratios implemented in this  
277 constructor, from <sup>20</sup>, are presented in the appendix (Table A1). In this constructor, for a complete  
278 simulation of water radiolysis, 15 molecular species listed in Table A2 are available (instead of 7  
279 for the SBS constructors <sup>44</sup>). In addition, the 72 chemical reactions listed in tables A3-A7 are  
280 available (instead of 9 for the step-by-step constructors <sup>45,46</sup>).

281

282 *Table 1 Chemistry constructors available in Geant4-DNA.*

<b>Geant4-DNA Constructor</b>	<b>Description</b>
<b>G4EmDNAChemistry</b>	First constructor implemented in Geant4-DNA for the chemistry processes with parameter values from Karamitros et al <sup>18,19</sup>
<b>G4EmDNAChemistry_option1</b>	Implements a revisited set of chemistry parameters used in Shin et al <sup>20</sup>
<b>G4EmDNAChemistry_option2</b>	Includes chemistry parameters for simulating reactions with DNA components.



**G4EmDNAChemistry\_option3**

Implements the IRT approach presented in this work.

283

### 284 *2.2.2 Computational efficiency.*

285 The computational efficiency  $\varepsilon$ , is a figure-of-merit that relates the computation time  $T$  spent to  
286 achieve a statistical variance,  $\sigma^2$ :

287

$$288 \quad \varepsilon = (T\sigma^2)^{-1}. \quad (8)$$

289

290 In this work,  $\varepsilon$  was used to compare the computational efficiency of SBS and our IRT  
291 methods for the calculation of radiolytic yields, both implemented in Geant4-DNA as explained  
292 above. Simulations using both methods were performed to reach the same  $\sigma^2$  for G-value  
293 calculations. We assume this can be achieved by simulating the same number of histories and  
294 using the same processes to model the physical (particle tracks) and pre-chemical (radiolysis)  
295 stages. The computational efficiency enhancement of the IRT over the SBS method was  
296 quantified by the reduced ratio  $\varepsilon_R$ , defined as the ratio between the computation times to  
297 simulate only the chemical stages,  $T_{SBS}$  and  $T_{IRT}$  with  $\sigma^2_{SBS} = \sigma^2_{IRT}$ , calculated as follows:

298

$$299 \quad \varepsilon_R = T_{SBS}T_{IRT}^{-1} \quad (9)$$

300

301 The quantity  $\varepsilon_R$  is reported as a function of the unrestricted linear energy transfer (LET),  
302 averaged over simulated short track segments of electrons, protons or alpha particles. LET was  
303 calculated as the accumulated energy deposited in the scoring region, including all secondary

304 electrons, divided by the primary track length <sup>47</sup>. For electrons, the simulation consisted of short  
305 track segments of initially monoenergetic electrons positioned at the center of a water cube of 1  
306 cm side. The transport of each primary electron was terminated immediately after its  
307 accumulated energy loss exceeds a specific energy cut. Secondary electrons produced by inelastic  
308 interactions were transported down to the lower energy cut of Geant4-DNA model limits, see  
309 section 2.2.1. That criteria and energy cut values are given elsewhere <sup>20,46</sup>. For protons and alpha  
310 particles, short tracks segments were generated by terminating the transport of the primary  
311 particle at a pre-defined length. For protons, the track lengths ranged from 2.5  $\mu\text{m}$  for the lowest  
312 energy value (0.5 MeV) to 20  $\mu\text{m}$  for the highest energy value (100 MeV). For alpha particles, a  
313 2.5  $\mu\text{m}$  length was used for all the energy values (1 MeV/u to 12.5 MeV/u). The secondary  
314 electrons were simulated down to the energy limits of the Geant4-DNA's ELSEPA model for elastic  
315 scattering at 7.4 eV, section 2.2.1 and <sup>40</sup>. Reference simulations, in terms of computational  
316 efficiency, were performed using the SBS method. For both IRT and SBS methods, 24 statistically  
317 independent simulations were run using the same CPU unit and the same number of primary  
318 histories, which ranged from 5 to 600 per simulation job for the highest-LET (alpha 4 MeV/u) and  
319 lowest-LET (electrons 1 MeV), respectively. Finally,  $\epsilon_R$  was calculated using equation 9 and  
320 reported as the mean with its statistical uncertainty at one standard deviation. In all the  
321 simulations, the statistical uncertainty of the chemical yields was better than 0.5%, one standard  
322 deviation.

323

324 *2.2.3 Time-dependent and LET-dependent G-values.*

325 The set of reactions used are listed in the Appendix section; see also section 2.1.1. Simulations  
326 performed to compare SBS with IRT used only those reactions available in SBS, as marked in the  
327 appendix section. The branching ratios for the dissociation of water molecules and electron  
328 attachment are described in section 2.2.1. The simulation setups are described in section 2.2.2.

329 The time evolution of chemical yields was calculated using the first 10 keV of energy loss  
330 from 1 MeV electron tracks, which is a conventional method to perform G-values calculation for  
331 fast electrons<sup>20,46–48</sup>. At the sub nanosecond scale, calculated results were presented along with  
332 direct measurements of G-values in water for  $\cdot\text{OH}$  and  $e^-_{\text{aq}}$  from electron beams obtained with  
333 picosecond pulse radiolysis reported by<sup>49 50 51</sup> and<sup>52</sup>. At the microsecond scale, G-values were  
334 calculated for comparison to those measured for electron beams from Muroya et al<sup>50</sup> and <sup>60</sup>Co  
335 irradiation from LaVerne<sup>53</sup> and Yoshida et al.<sup>54</sup>

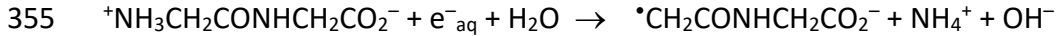
336 For LET-dependent yields, G-values at 1  $\mu\text{s}$  were calculated for comparison to compiled  
337 experimental data. In most of the experimental LET data, measurements were obtained in the  
338 presence of scavengers, while the calculations were performed in pure water. A suitable  
339 comparison requires reproducing the experimental conditions in the simulation as best as  
340 possible, for example, simulating the same scavenger system used in each experiment. The  
341 objective of this work was to verify the reproducibility of the behavior of the chemical yields as  
342 the ionization density increases.

343

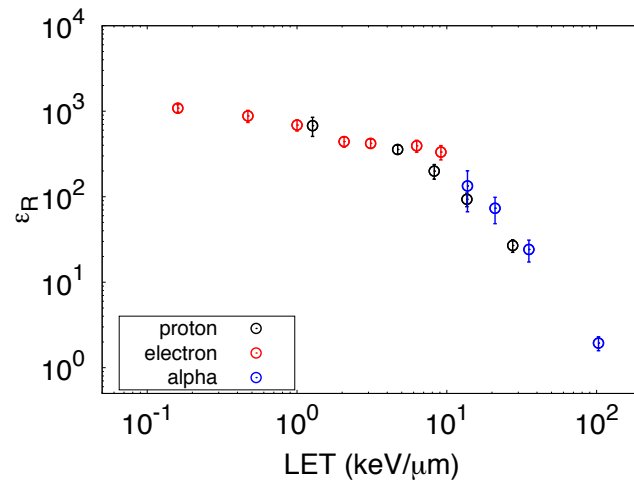
344 *2.2.4 G-value calculation in the presence of scavengers.*

345 The capability of the IRT implementation to model the presence of scavengers was verified for 1  
346 MeV electrons (first 10 keV of energy deposited) and 2 MeV protons. The feature to simulate  
347 scavengers with the Geant4-DNA SBS was not available at this point. Simulations of the system  
348 containing glycylglycine at concentrations ranging from  $10^{-4}$  M to 1 M (1 M = 1 mol dm<sup>-3</sup>) were  
349 performed by adding the set of reactions (R1-R3). The bulk medium was made of liquid water ( $\rho$   
350 = 1 g cm<sup>-3</sup>) at neutral pH and ambient temperature. The yield of produced ammonium cation NH<sub>4</sub><sup>+</sup>  
351 from the scavenging of e<sup>-</sup><sub>aq</sub> was calculated at the end of the chemical stage and compared with  
352 experimental values for a range of scavenger capacities from Yoshida et al.<sup>54</sup> for  $\gamma$ -rays and from  
353 LaVerne<sup>55</sup> for protons.

354



361



363

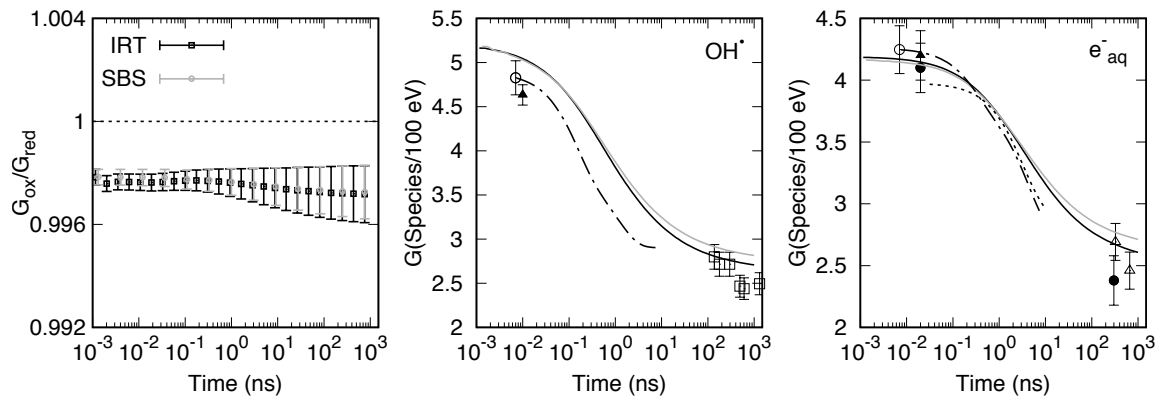
364 *Figure 4: LET-dependent computational efficiency of IRT implemented in Geant4-DNA relative to the SBS method. Results are*  
 365 *shown for electrons (red), protons (black) and alpha particles (blue). Error bars represent one standard deviation of statistical*  
 366 *uncertainty.*

367

### 368 3.1 Computational efficiency.

369 In Figure 4,  $\epsilon_R$  is shown as a function of LET for simulations with the IRT method implemented in  
 370 Geant4-DNA, calculated as the ratio of time taken in the chemistry portion of the simulation using  
 371 SBS and IRT for the same calculation precision (Equation 9). A substantial efficiency improvement  
 372 of three orders of magnitude was achieved with the IRT method implemented in Geant4-DNA for  
 373 the lower LET electron and proton simulations. As the LET increases for the electron source,  $\epsilon_R$  is  
 374 reduced to a still significant factor of two.

375



376

377 *Figure 5: Calculated time dependent ratio between oxidative and reductive G-Values from the first 10 keV energy deposited by 1*  
 378 *MeV electrons (left) from Geant4 IRT (black points) and SBS (light gray points). Error bars represent combined statistical*  
 379 *uncertainty, one standard deviation. Time-depended G-values for  $\text{OH}^\bullet$  radical (center) and solvated electron (right) from IRT (black*  
 380 *lines) and SBS (light gray lines). Experimental data from pulse radiolysis are shown at shorter times with filled triangles<sup>51</sup>, empty*  
 381 *circles and dotted-dashed lines<sup>52</sup>, dot-dashed lines<sup>49</sup> (using a time correlation method) and filled circles<sup>50</sup>. At longer times, data*  
 382 *from  $^{60}\text{Co}$  irradiations are shown with empty squares<sup>53</sup>, filled circles<sup>50</sup> and empty triangles<sup>54</sup>. Experimental errors represent one*  
 383 *standard deviation.*

384

### 385 3.2 Time-dependent and LET-dependent G-value.

#### 386 *Time-dependent G-values.*

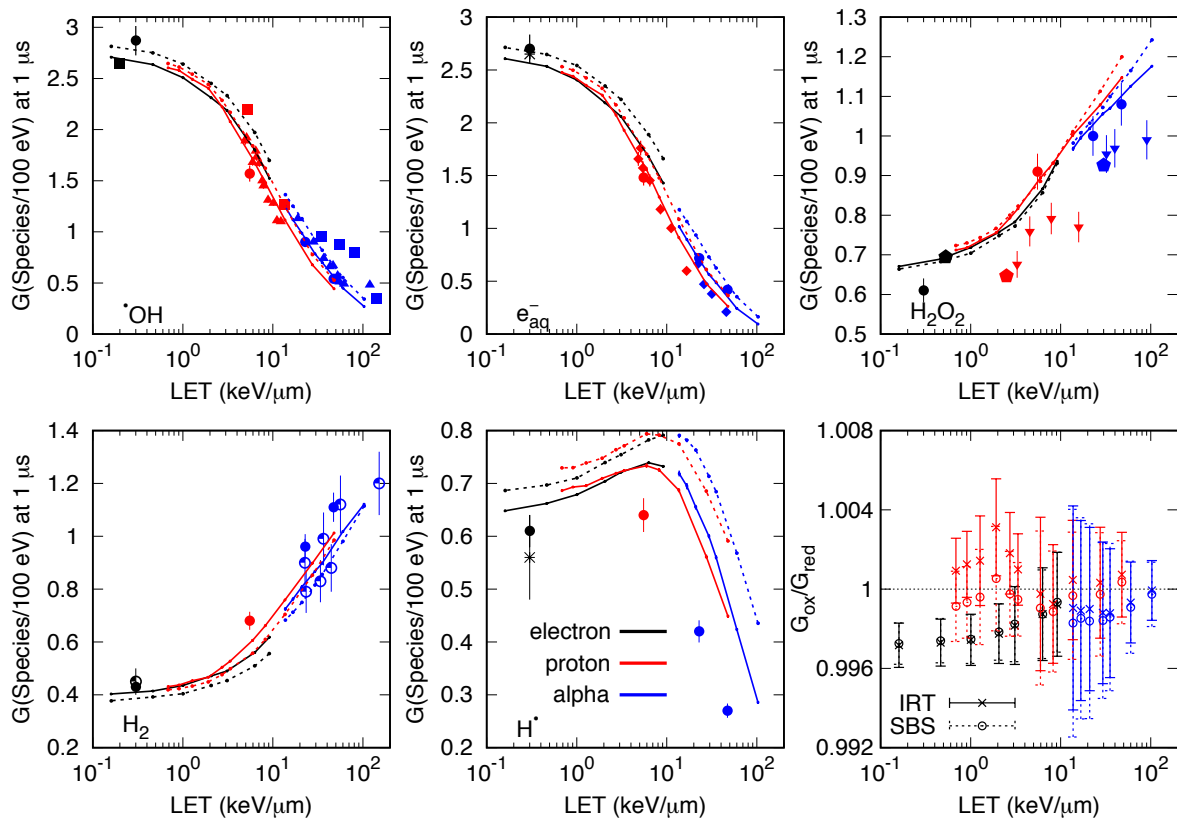
387 Figure 5 shows the time-dependent yields for the first 10 keV of energy deposited along 1 MeV  
 388 electron tracks. From the graph on the left of the figure, it is shown that the material balance  
 389 equation for oxidizing ( $\text{OH}^\bullet$  and  $\text{H}_2\text{O}_2$ ) and reducing ( $e^-_{aq}$ ,  $\text{H}^\bullet$  and  $\text{H}_2$ ) species is (almost) fulfilled  
 390 with a statistically significant systematic deviation of 0.3% for both IRT and SBS implementations.

391 Figure 5 also shows the time-dependent G-value for  $\text{OH}^\bullet$  radical and  $e^-_{aq}$ . At the shorter  
 392 times, IRT and SBS calculations agreed within combined statistical uncertainties, as the same

393 physics models and pre-chemical dissociative channels were used. At longer times, IRT differed  
394 from SBS by up to  $-3.8\% \pm 0.1\%$ , and  $-3.9\% \pm 0.1\%$  for  $\cdot\text{OH}$  and  $e^-_{\text{aq}}$ , respectively.

395 For  $\cdot\text{OH}$ , direct measurements from irradiations of electrons in pure water for the shorter  
396 time range ( $< 10$  ns) from El Omar et al.<sup>51</sup> and Wang et al.<sup>52</sup> are shown. The magnitude of the  
397 experimental error is shown at a single time of  $10^{-2}$  ns for clarity. The obtained decay of  $\cdot\text{OH}$  yields  
398 from  $7 \times 10^{-3}$  ns to 8 ns for both IRT and SBS methods exceed the more recent experimental yields  
399 from Wang et al.<sup>52</sup> at  $7 \times 10^{-3}$  ns by  $0.3 \pm 0.12$  molec./100 eV, one standard deviation. At  $10^3$  ns,  
400 IRT and SBS exceed the experimental data by  $0.22 \pm 0.12$  molec./100 eV and  $0.32 \pm 0.12$   
401 molec./100 eV, one standard deviation, respectively.

402 For solvated electrons, at the earliest times both IRT and SBS calculations agreed with  
403 direct measurements from Bartels et al.<sup>49</sup>, El Omar et al.<sup>51</sup> and Wang et al.<sup>52</sup>, within one standard  
404 deviation of the experimental error. At longer times, calculated data from both methods agreed  
405 with the experimental data from Yoshida et al.<sup>54</sup> within one standard deviation.



406

407 *Figure 6: Unrestricted LET-dependent G-values at 1 μs for electrons (black), protons (red) and alpha particles (blue). IRT*  
 408 *calculations are shown with solid lines connecting crosses and SBS are shown with dotted lines connecting empty circles.*  
 409 *Experimental data from γ-rays (black), proton or deuteron (red) and alpha particles (blue) are shown with symbols: filled square<sup>56</sup>,*  
 410 *filled circle<sup>57</sup>, filled triangle<sup>58</sup>, filled diamond<sup>59</sup>, star<sup>60</sup>, inverted triangle<sup>61</sup>, filled polygon<sup>62</sup>, and semi filled circle<sup>63</sup>. Experimental*  
 411 *error bars represent one standard deviation. The LET-dependent ratio between oxidative and reduction species is shown at the*  
 412 *bottom right panel. Error bars represent combined statistical uncertainty, one standard deviation.*

413 *LET-dependent G-values.*

414 Figure 6 shows the LET-dependent G-value for electrons, protons and alpha particles calculated  
 415 with IRT and SBS. The material balance equation, represented as the ratio between oxidative to  
 416 reduced species as a function of the LET, is shown in the bottom right of Figure 6. The ratio  
 417 reaches unity within statistical uncertainties for protons and alpha particles, but deviates from  
 418 unity by 0.3% for electrons, as seen in Figure 6. Measured data from the literature are also

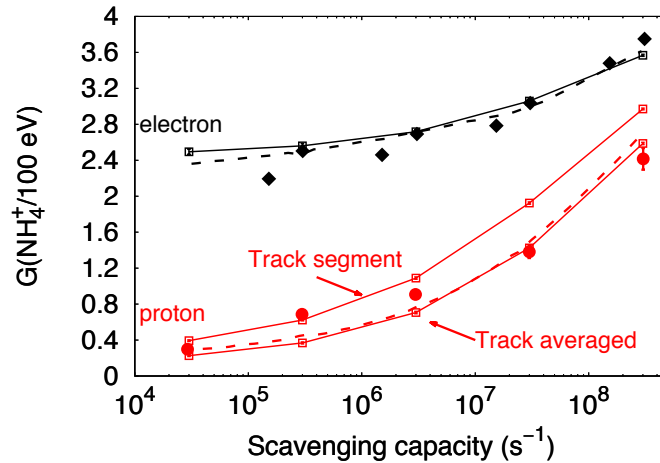


419 displayed from different particles. For the chemical species displayed in Figure 6, the calculated  
420 yields reproduce the change in the experimental data as the LET increases. That is, although the  
421 yield of  $H^*$  and  $H_2O_2$  are significantly higher in the simulation than the experiments, the slope of  
422 the yield with LET is in reasonable agreement.

423

#### 424 *G-value calculation in the presence of scavengers.*

425 Modeling the presence of scavengers is shown in Figure 7 for the yield of  $NH_4^+$  produced by  
426 electrons and protons as a function of the scavenging capacity. For electrons, calculated data  
427 from LaVerne et al <sup>55</sup> using IRT is also shown. The experimental data from cobalt-60  $\gamma$ -rays  
428 irradiation, which result in a scavenging capacity comparable to electrons, is from Yoshida et al  
429 <sup>54</sup>. As shown, a consistent agreement of the behavior of  $NH_4^+$  yields is fairly reproduced by the  
430 Geant4-DNA implementation of IRT. For low energy protons, measured data are reported as  
431 track-averaged G-values while the IRT calculation is typically calculated with track-segment G-  
432 value, which is calculated over an almost constant LET across a short track-segment. The  
433 comparison of both track-segment and track-averaged G-values are shown in Figure 7. The track-  
434 averaged G-values were obtained by integrating the G-values from short proton track-segments  
435 from 2 MeV to 0.1 MeV, the limit of the Geant4-DNA models for protons. Results are consistent  
436 with calculated data from LaVerne et al <sup>55</sup> where the G-values are also reported as a track-  
437 averaged quantity.



438

439 *Figure 7 : Calculated  $\text{NH}_4^+$  yields with Geant4-DNA IRT (empty squares connected with solid lines) and from LaVerne<sup>55</sup> (dashed*  
 440 *lines) at different scavenging capacities of glycylglycine. Electron irradiation (black) simulations are compared to measured data*  
 441 *for cobalt-60 from Yoshida et al<sup>54</sup> (solid diamonds). Data for 2 MeV proton (red) simulations are compared to measured data*  
 442 *from LaVerne<sup>55</sup> (filled circles.) For protons, both track-segment and track-averaged G-values are shown.*

443

#### 444 4 Discussion.

445 In this work, an implementation of the independent reaction times (IRT) in Geant4-DNA was  
 446 presented. A substantial improvement in the computational efficiency was achieved, up to three  
 447 orders of magnitude at low LET, decreasing as the particle LET increases. This decrease was  
 448 caused by the increase in the density of ionized and excited events from high LET particles  
 449 compared to low LET particles. As a consequence, the increased number of neighbor initial  
 450 chemical species looked by the IRT searching algorithm, as implemented, demanded more  
 451 operations as the complexity of this algorithm is  $O(N(N-1)/2)$ . Thus, degrading in the efficiency  
 452 with increasing the LET was expected. Implementing a neighbor searching algorithm, for  
 453 example, by adopting the kd-tree algorithm available in Geant4-DNA<sup>19</sup>, and the implementation

454 of a cutoff distance <sup>25</sup> as a function of the LET, will potentially mitigate such reduction in  
455 efficiency.

456 A systematic deviation of 0.3% from unity was found for the ratio between oxidative  
457 species to reduced species for electron tracks calculated with both SBS and IRT. The difference  
458 might be caused by the lack of dissociation scheme of the double ionized water molecules  
459 induced by Auger electrons produced by our implementation of the physics list, but are currently  
460 considered as single ionized water molecules in our simulation. However, this discrepancy is well  
461 below the experimental uncertainty of 5% typically reported, shown in the center and right  
462 panels of Figure 5, and is thus results in a negligible systematic error.

463 For time-dependent G-values a clear difference was found between IRT and SBS at longer  
464 times, hence, also reflected in LET-dependent G-values. The differences might be attributed in  
465 part to the independent pair approximation taken by the IRT approach whereas the SBS considers  
466 a multiparticle system <sup>64</sup>. Nevertheless, it has been shown that the yields calculated with SBS are  
467 equivalent to IRT when using two-particle systems <sup>3,24,65</sup>. In addition, the G-values calculated with  
468 the SBS approach depended to some extent on the minimum time step which is implemented in  
469 a dynamic time partition<sup>19</sup>. To quantify this effect, we calculated G-values for <sup>•</sup>OH produced by 1  
470 MeV electrons using a fixed minimum time step to 0.1 ps. While the G-value for solvated  
471 electrons remained unaffected, our results showed that the G-value for <sup>•</sup>OH reduced by 2.6% at  
472 1 μs when the fixed minimum time step was used instead of the default values used by the  
473 dynamic time step (see table 4 in Karamitros et al <sup>18</sup>). However, we kept the latter time step  
474 configuration in all the simulations because the systematic difference, smaller than reported

475 experimental errors, was tolerated given the computational overhead of four-fold introduced by  
476 the use of a small-time step.

477 A significant overestimate of G-values, outside the experimental error of the latest  $\cdot\text{OH}$   
478 measurements from Wang et al<sup>52</sup>, was found for both SBS and IRT at  $10^{-2}$  ns. The data from Wang  
479 et al is the most recent data obtained at the shortest time following irradiation (7 ps). To resolve  
480 this mismatch, a comprehensive revision of the current physical and water dissociative schemes  
481 implemented in Geant4-DNA, following Wang et al<sup>52</sup> data, is encouraged. That revision task is an  
482 ongoing work within our group that began with the revision of the physical models as reported  
483 recently<sup>20</sup>. We expect that the revision of physical and pre-chemical processes also has a good  
484 impact in the Geant4-DNA accuracy at the steady state ( $10^3$  ns), where currently a reasonable  
485 agreement is found. Nevertheless, for  $e^-_{\text{aq}}$  a satisfactory agreement was found within the  
486 experimental error over the entire time domain.

487 The evolution of G-values as a function of the particle LET were reproduced by both SBS  
488 and IRT. The magnitude of the calculated yields was in reasonable agreement with measured  
489 data for most of the species, considering the experimental uncertainties, and considering that  
490 the measurements were performed in the presence of scavengers, while calculations were  
491 performed in pure liquid water. A strict comparison between calculated and measured data  
492 requires strict adherence to the experimental conditions in the simulations, including the  
493 presence of scavengers, the comparison of track-averaged and track-segment G-values (Figure  
494 5), and the implementation of the multiple ionization process, shown to improve the accuracy  
495 for  $\text{H}_2\text{O}_2$  in the high LET range<sup>28,66</sup>.

## 496 5 Conclusions.

497 In this work, the Independent Reaction Times method that simulates the reaction kinetics  
498 following the interaction of ionizing radiation was successfully implemented in Geant4-DNA. The  
499 implementation achieves a substantial computational efficiency over the existing step-by-step  
500 method (SBS) of Geant4-DNA by up to three orders of magnitude. Both methods achieve similar  
501 accuracy when compared to experimental data of time-dependent and LET-dependent G-values.  
502 The lack of consideration of partially diffusion-controlled reactions in the SBS with the selection  
503 of a dynamic time step resolution causes a difference in G-values by 3.9% with respect to IRT data  
504 at 1  $\mu$ s. The capabilities of simulating systems with scavengers was demonstrated and showed  
505 satisfactory agreement with experimental data. However, for  $\cdot$ OH radical yields, there was a  
506 significant overestimate of 5% at the earliest time (7 ps) from recently measured yields. Further  
507 work to resolve such differences is ongoing within our group. The implementation presented  
508 here is a step forward to facilitate such studies.

## 509 Acknowledgments.

510 We are grateful to Dr. Ianik Plante from NASA for his invaluable discussion on the sampling  
511 methodologies. To Prof. Mehran Mostafavi from CNRS/Université Paris-Sud for providing with  
512 the latest references of measured G-values. To Prof. Jay LaVerne from University of Notre Dame  
513 for his invaluable discussion and motivation of the current work. JRM acknowledges funding from  
514 a UCSF Medical School Bridge Funding grant and NIH R01 CA187003 (TOPAS-nBio). NDK is a  
515 doctoral student from Programa de Doctorado en Física Aplicada, Benemérita Universidad  
516 Autónoma de Puebla (BUAP) and received national fellowship from CONACYT. WGS and SI thank

517 the University of Bordeaux Initiative of Excellence International Doctorates program in the  
 518 framework of the “France-Korea Particle Physics Laboratory” International Associated Laboratory  
 519 (2017– 2020), as well as CNRS/IN2P3 for the “MOVI” Master Project structuring action.

520 [Appendix A](#)

521 The list of reactions available in the Geant4-DNA IRT implementation are shown in Tables A1 to  
 522 A4. The classification is that proposed by Frongillo et al <sup>5</sup>. The reaction rate coefficients are  
 523 from Plante and Devroye <sup>3</sup>. The molar concentration M is equal to 1 mol dm<sup>-3</sup>

524

525

526 *Table A1 Molecular dissociation scheme and branching ratios available in the “G4DNAChecker\_option3” chemistry constructor*

527 <sup>20</sup>.

Physical interaction	Scheme	Dissociation products	Probability
Ionization	Dissociation	$\text{H}_3\text{O}^+ + \cdot\text{OH}$	1
Excitation (A1B1)	Dissociation	$\cdot\text{OH} + \text{H}^{\cdot}$	0.65
	Relaxation	$\text{H}_2\text{O} + \Delta\text{E}$	0.35
Excitation (B1A1)	Auto- ionization	$\text{H}_3\text{O}^+ + \cdot\text{OH} + e_{\text{aq}}^-$	0.55
	Dissociation	$\cdot\text{OH} + \cdot\text{OH} + \text{H}_2$	0.15
	Relaxation	$\text{H}_2\text{O} + \Delta\text{E}$	0.3
Excitation (Rydberg, diffuse bands)	Auto- ionization	$\text{H}_3\text{O}^+ + \cdot\text{OH} + e_{\text{aq}}^-$	0.5
	Relaxation	$\text{H}_2\text{O} + \Delta\text{E}$	0.5
Dissociative attachment ( $\text{H}_2\text{O}^{\cdot-}$ )	Dissociation	$\cdot\text{OH} + \text{OH}^- + \text{H}_2$	1

Recombination electron-hole	Dissociation	$\cdot\text{OH} + \cdot\text{OH} + \text{H}_2$	0.15
	Dissociation	$\cdot\text{OH} + \text{H}\cdot$	0.55
	Relaxation	$\text{H}_2\text{O} + \Delta\text{E}$	0.3

528

529

530 *Table A2 Molecular species, diffusion coefficients and radii used for radiolysis simulation with IRT, from <sup>3</sup>. \*Available in the SBS*

531 *constructors and used also in IRT for the comparison studies of this work.*

<b>Molecular species</b>	<b>Diffusion coefficient (<math>10^9\text{nm}^2\text{s}^{-1}</math>)</b>	<b>Radius (nm)</b>
$\text{H}\cdot$	7.0*	0.19
$\cdot\text{OH}$	2.2*	0.22
$\text{H}_2\text{O}_2$	2.3*	0.21
$\text{H}_2$	4.8*	0.14
$\text{e}^-_{\text{aq}}$	4.9*	0.50
$\text{H}_3\text{O}^+$	9.46*	0.25
$\text{OH}^-$	5.3*	0.33
$\text{O}_2$	2.4	0.17
$\text{O}_2^{\cdot-}$	1.75	0.22
$\text{HO}\cdot_2$	2.3	0.21
$\text{HO}_2^-$	1.4	0.25
$\text{O}(^3\text{P})$	2.0	0.20
$\text{O}^{\cdot-}$	2.0	0.25
$\text{O}_3^{\cdot-}$	2.0	0.20
$\text{O}_3$	2.0	0.20

532

533

534 Table A3 Totally-diffusion controlled reactions where at least one neutral particle is involved. Shaded reactions are used for the  
 535 comparison studies of this work.

Reaction type I	$k_{\text{obs}}$ (/M/s)
$\text{H}^\bullet + \text{e}^-_{\text{aq}} \rightarrow \text{H}_2 + \text{OH}^-$	$2.50 \times 10^{10}$
$\text{H}^\bullet + \text{H}^\bullet \rightarrow \text{H}_2$	$5.03 \times 10^9$
$\text{H}^\bullet + \text{O}(\text{}^3\text{P}) \rightarrow \text{}^\bullet\text{OH}$	$2.02 \times 10^{10}$
$\text{}^\bullet\text{OH} + \text{O}(\text{}^3\text{P}) \rightarrow \text{HO}_2$	$2.02 \times 10^{10}$
$\text{H}^\bullet + \text{O}^{\bullet-} \rightarrow \text{OH}^-$	$2.00 \times 10^{10}$
$\text{HO}_2 + \text{O}(\text{}^3\text{P}) \rightarrow \text{O}_2 + \text{}^\bullet\text{OH}$	$2.02 \times 10^{10}$
$\text{O}(\text{}^3\text{P}) + \text{O}(\text{}^3\text{P}) \rightarrow \text{O}_2$	$2.20 \times 10^{10}$

536  
 537 Table A4 Partially-diffusion controlled reactions where at least one neutral particle is involved. Shaded reactions are used for the  
 538 comparison studies of this work.

Reaction type II	$k_{\text{obs}}$ (/M/s)	$k_{\text{diff}}$ (/M/s)	$k_{\text{act}}$ (/M/s)
$\text{}^\bullet\text{OH} + \text{e}^-_{\text{aq}} \rightarrow \text{OH}^-$	$2.95 \times 10^{10}$	$3.87 \times 10^{10}$	$1.24 \times 10^{11}$
$\text{}^\bullet\text{OH} + \text{}^\bullet\text{OH} \rightarrow \text{H}_2\text{O}_2$	$5.50 \times 10^9$	$7.33 \times 10^9$	$2.21 \times 10^{10}$
$\text{}^\bullet\text{OH} + \text{OH}^- \rightarrow \text{O}^{\bullet-} + \text{H}_2\text{O}$	$6.30 \times 10^9$	$3.12 \times 10^{10}$	$7.89 \times 10^9$
$\text{}^\bullet\text{OH} + \text{HO}_2^- \rightarrow \text{HO}_2^\bullet + \text{OH}^-$	$8.32 \times 10^9$	$1.28 \times 10^{10}$	$2.38 \times 10^{10}$
$\text{}^\bullet\text{OH} + \text{O}^{\bullet-} \rightarrow \text{HO}_2^-$	$1.00 \times 10^9$	$1.49 \times 10^{10}$	$1.07 \times 10^9$
$\text{}^\bullet\text{OH} + \text{HO}_2^\bullet \rightarrow \text{O}_2 + \text{H}_2\text{O}$	$7.90 \times 10^9$	$1.46 \times 10^{10}$	$1.72 \times 10^{10}$
$\text{}^\bullet\text{OH} + \text{H}_2\text{O}_2 \rightarrow \text{HO}_2^\bullet + \text{H}_2\text{O}$	$2.88 \times 10^7$	$1.46 \times 10^{10}$	$2.89 \times 10^7$
$\text{}^\bullet\text{OH} + \text{H}_2 \rightarrow \text{H}^\bullet + \text{H}_2\text{O}$	$3.28 \times 10^7$	$1.91 \times 10^{10}$	$3.29 \times 10^7$
$\text{}^\bullet\text{OH} + \text{O}_2^{\bullet-} \rightarrow \text{O}_2 + \text{OH}^-$	$1.07 \times 10^{10}$	$1.32 \times 10^{10}$	$5.74 \times 10^{10}$
$\text{}^\bullet\text{OH} + \text{O}_3^{\bullet-} \rightarrow \text{O}_2^{\bullet-} + \text{HO}_2^\bullet$	$8.50 \times 10^9$	$1.34 \times 10^{10}$	$2.34 \times 10^{10}$
$\text{H}^\bullet + \text{}^\bullet\text{OH} \rightarrow \text{H}_2\text{O}$	$1.55 \times 10^{10}$	$2.86 \times 10^{10}$	$3.39 \times 10^{10}$
$\text{H}^\bullet + \text{OH}^- \rightarrow \text{e}^-_{\text{aq}} + \text{H}_2\text{O}$	$2.51 \times 10^7$	$4.84 \times 10^{10}$	$2.51 \times 10^7$
$\text{e}^-_{\text{aq}} + \text{H}_2\text{O}_2 \rightarrow \text{OH}^- + \text{}^\bullet\text{OH}$	$1.10 \times 10^{10}$	$3.87 \times 10^{10}$	$1.54 \times 10^{10}$



$e^-_{aq} + HO_2^* \rightarrow HO_2^-$	$1.29 \times 10^{10}$	$3.87 \times 10^{10}$	$1.94 \times 10^{10}$
$e^-_{aq} + O_2 \rightarrow O_2^{*-}$	$1.74 \times 10^{10}$	$3.70 \times 10^{10}$	$3.28 \times 10^{10}$
$H_2O_2 + OH^- \rightarrow HO_2^- + H_2O$	$4.71 \times 10^8$	$3.11 \times 10^{10}$	$4.78 \times 10^8$
$H_2O_2 + O_3(P) \rightarrow HO_2^* + ^*OH$	$1.60 \times 10^9$	$1.33 \times 10^{10}$	$1.82 \times 10^9$
$H_2O_2 + O^{*-} \rightarrow HO_2^* + OH^-$	$5.55 \times 10^8$	$1.50 \times 10^{10}$	$5.76 \times 10^8$
$H^* + HO_2^* \rightarrow H_2O_2$	$1.00 \times 10^{10}$	$2.82 \times 10^{10}$	$1.55 \times 10^{10}$
$H^* + H_2O_2 \rightarrow ^*OH + H_2O$	$3.50 \times 10^7$	$2.82 \times 10^{10}$	$3.50 \times 10^7$
$H^* + O_2 \rightarrow HO_2^*$	$2.10 \times 10^{10}$	$2.56 \times 10^{10}$	$1.17 \times 10^{11}$
$H^* + O_2^- \rightarrow HO_2^-$	$1.00 \times 10^{10}$	$2.72 \times 10^{10}$	$1.58 \times 10^{10}$
$H_2 + O_3(P) \rightarrow H^* + ^*OH$	$4.77 \times 10^3$	$1.75 \times 10^{10}$	$4.77 \times 10^3$
$H_2 + O^{*-} \rightarrow H^* + OH^-$	$1.21 \times 10^8$	$2.01 \times 10^{10}$	$1.22 \times 10^8$
$OH^- + HO_2^* \rightarrow O_2^{*-} + H_2O$	$6.30 \times 10^9$	$3.11 \times 10^{10}$	$7.90 \times 10^9$
$OH^- + O_3(P) \rightarrow HO_2^-$	$4.20 \times 10^8$	$2.93 \times 10^{10}$	$4.26 \times 10^8$
$O_2 + O_3(P) \rightarrow O_3$	$4.00 \times 10^9$	$1.23 \times 10^{10}$	$5.92 \times 10^9$
$O_2 + O^{*-} \rightarrow O_3^{*-}$	$3.70 \times 10^9$	$1.40 \times 10^{10}$	$5.03 \times 10^9$
$HO_2^* + HO_2^* \rightarrow H_2O_2 + O_2$	$9.80 \times 10^5$	$7.31 \times 10^9$	$9.80 \times 10^5$
$HO_2^* + O_2^{*-} \rightarrow HO_2^- + O_2$	$9.70 \times 10^7$	$1.32 \times 10^{10}$	$9.77 \times 10^7$
$HO_2^- + O_3(P) \rightarrow O_2^{*-} + ^*OH$	$5.30 \times 10^9$	$1.16 \times 10^{10}$	$9.77 \times 10^9$

539

540 *Table A5 Totally-diffusion controlled reactions between charged chemical species. Shaded reactions are used for the comparison*541 *studies of this work.*

Reaction type III	$k_{obs}$ (/M/s)
$e^-_{aq} + e^-_{aq} \rightarrow H_2 + OH^-$	$6.36 \times 10^9$
$H_3O^+ + OH^- \rightarrow H_2O$	$1.13 \times 10^{11}$
$H_3O^+ + O_3^{*-} \rightarrow ^*OH + O_2$	$8.99 \times 10^{10}$

542

543 *Table A6 Partially-diffusion controlled reactions between charged chemical species. Shaded reactions are used for the*  
 544 *comparison studies of this work.*

Reaction type IV	$k_{\text{obs}}$ (/M/s)	$k_{\text{diff}}$ (/M/s)	$k_{\text{act}}$ (/M/s)
$e^-_{\text{aq}} + \text{H}_3\text{O}^+ \rightarrow \text{H}^*$	$2.11 \times 10^{10}$	$1.26 \times 10^{11}$	$2.53 \times 10^{10}$
$e^-_{\text{aq}} + \text{O}^- \rightarrow 2 \text{OH}^-$	$2.31 \times 10^{10}$	$2.35 \times 10^{10}$	$1.44 \times 10^{12}$
$e^-_{\text{aq}} + \text{O}_2^{\bullet-} \rightarrow \text{H}_2\text{O}_2 + 2 \text{OH}^-$	$1.29 \times 10^{10}$	$2.12 \times 10^{10}$	$3.29 \times 10^{10}$
$e^-_{\text{aq}} + \text{HO}_2^- \rightarrow \text{O}^{\bullet-} + \text{OH}^-$	$3.51 \times 10^9$	$2.14 \times 10^{10}$	$4.20 \times 10^9$
$\text{H}_3\text{O}^+ + \text{HO}_2^- \rightarrow \text{H}_2\text{O}_2$	$5.00 \times 10^{10}$	$7.71 \times 10^{10}$	$1.42 \times 10^{11}$
$\text{H}_3\text{O}^+ + \text{O}^- \rightarrow \text{OH}^*$	$4.78 \times 10^{10}$	$8.13 \times 10^{10}$	$1.16 \times 10^{11}$
$\text{H}_3\text{O}^+ + \text{O}_2^{\bullet-} \rightarrow \text{HO}_2^*$	$4.78 \times 10^{10}$	$7.74 \times 10^{10}$	$1.25 \times 10^{11}$
$\text{O}^{\bullet-} + \text{O}^{\bullet-} \rightarrow \text{H}_2\text{O}_2 + 2 \text{OH}^-$	$1.00 \times 10^8$	$3.42 \times 10^9$	$1.03 \times 10^8$
$\text{O}^{\bullet-} + \text{O}_3^{\bullet-} \rightarrow 2 \text{O}_2^{\bullet-}$	$7.01 \times 10^8$	$5.58 \times 10^9$	$8.00 \times 10^8$
$\text{O}^{\bullet-} + \text{O}_2^{\bullet-} \rightarrow \text{O}_2 + 2 \text{OH}^-$	$6.00 \times 10^8$	$5.70 \times 10^9$	$6.71 \times 10^8$
$\text{O}^{\bullet-} + \text{HO}_2^- \rightarrow \text{O}_2^{\bullet-} + \text{OH}^-$	$3.50 \times 10^8$	$5.81 \times 10^9$	$3.72 \times 10^8$

545  
 546 *Table A7 Reactions with  $\text{H}_2\text{O}$ ,  $\text{H}_3\text{O}^+$  and  $\text{OH}^-$  (scavenging capacity is provided), and first order reactions (reaction rate constant*  
 547  *$k_{\text{obs}}$  provided) available in Geant4-DNA, but not used in comparison studies of this work.*

Reaction	Scavenging capacity ( $\text{s}^{-1}$ ) or $k_{\text{obs}}$
$e^-_{\text{aq}} + \text{H}_2\text{O} \rightarrow \text{H}^* + \text{OH}^-$	$1.58 \times 10^{11}$
$\text{O}^- + \text{H}_2\text{O} \rightarrow \text{OH}^* + \text{OH}^-$	$1.36 \times 10^6$
$\text{HO}_2^- + \text{H}_2\text{O} \rightarrow \text{H}_2\text{O}_2 + \text{OH}^-$	$1.36 \times 10^6$
$\text{O}_2^{\bullet-} + \text{H}_2\text{O} \rightarrow \text{HO}_2^* + \text{OH}^-$	$1.50 \times 10^{-1}$
$\text{H}^* + \text{H}_2\text{O} \rightarrow e^-_{\text{aq}} + \text{H}_3\text{O}^+$	5.94
$\text{O}_3(\text{P}) + \text{H}_2\text{O} \rightarrow 2 \text{OH}^*$	$1.90 \times 10^3$
$\text{O}_2^{\bullet-} + \text{H}_3\text{O}^+ \rightarrow \text{HO}_2^*$	$4.73 \times 10^3$
$\text{O}_3^{\bullet-} + \text{H}_3\text{O}^+ \rightarrow \text{OH}^* + \text{O}_2$	$8.90 \times 10^3$
$e^-_{\text{aq}} + \text{H}_3\text{O}^+ \rightarrow \text{H}^*$	$2.09 \times 10^3$
$\text{HO}_2^- + \text{H}_3\text{O}^+ \rightarrow \text{H}_2\text{O}_2$	$4.95 \times 10^3$
$\text{OH}^- + \text{H}_3\text{O}^+ \rightarrow \text{H}_2\text{O}$	$1.12 \times 10^4$
$\text{O}^{\bullet-} + \text{H}_3\text{O}^+ \rightarrow \text{OH}^*$	$4.73 \times 10^3$

$\text{H}^{\bullet} + \text{OH}^{-} \rightarrow \text{e}^{-}_{\text{aq}} + \text{H}_2\text{O}$	2.49
$\text{OH}^{\bullet} + \text{OH}^{-} \rightarrow \text{O}^{\bullet-} + \text{H}_2\text{O}$	$6.24 \times 10^2$
$\text{H}_2\text{O}_2 + \text{OH}^{-} \rightarrow \text{HO}_2^{-} + \text{H}_2\text{O}$	$4.66 \times 10^1$
$\text{HO}_2^{\bullet} + \text{OH}^{-} \rightarrow \text{O}_2^{\bullet-} + \text{H}_2\text{O}$	$6.24 \times 10^2$
$\text{O}_3(\text{P}) + \text{OH}^{-} \rightarrow \text{HO}_2^{-}$	$4.16 \times 10^1$
$\text{O}_3^{\bullet-} \rightarrow \text{O}^{\bullet-} + \text{O}_2$	$2.66 \times 10^3$
$\text{HO}_2^{\bullet} \rightarrow \text{H}_3\text{O}^{+} + \text{O}_2^{\bullet-}$	$7.15 \times 10^5$

548

549 [References.](#)

- 550 1. Nikjoo H, Emfietzoglou D, Liamsuwan T, Taleei R, Liljequist D, Uehara S. Radiation track,  
551 DNA damage and response—a review. *Reports Prog Phys.* 2016;79(11):116601.  
552 doi:10.1088/0034-4885/79/11/116601
- 553 2. Dingfelder M, Hantke D, Inokuti M, Paretzke HG. Electron inelastic-scattering cross  
554 sections in liquid water. *Radiat Phys Chem.* 1999;53(1):1-18. doi:10.1016/S0969-  
555 806X(97)00317-4
- 556 3. Plante I, Devroye L. Considerations for the independent reaction times and step-by-step  
557 methods for radiation chemistry simulations. *Radiat Phys Chem.* 2017;139(September  
558 2016):157-172. doi:10.1016/j.radphyschem.2017.03.021
- 559 4. Boscolo D, Krämer M, Durante M, Fuss MC, Scifoni E. TRAX-CHEM: A pre-chemical and  
560 chemical stage extension of the particle track structure code TRAX in water targets.  
561 *Chem Phys Lett.* 2018;698:11-18. doi:10.1016/j.cplett.2018.02.051
- 562 5. Frongillo Y, Goulet T, Fraser M-J, Cobut V, Patau JP, Jay-Gerin J-P. Monte Carlo Simulation  
563 of Fast Electron And Proton Tracks In Liquid Water - II. Nonhomogeneous Chemistry.  
564 *Radiat Phys Chem.* 1998;51(3):245-254. doi:10.1016/S0969-806X(97)00097-2
- 565 6. Incerti S, Baldacchino G, Bernal M, et al. THE Geant4-DNA project. *Int J Model Simulation,*

- 566 *Sci Comput.* 2010;1(2):157-178. doi:10.1142/S1793962310000122
- 567 7. Incerti S, Ivanchenko A, Karamitros M, et al. Comparison of GEANT4 very low energy  
568 cross section models with experimental data in water. *Med Phys.* 2010;37(9):4692-4708.  
569 doi:10.1118/1.3476457
- 570 8. Bernal MA, Bordage MC, Brown JMC, et al. Track structure modeling in liquid water: A  
571 review of the Geant4-DNA very low energy extension of the Geant4 Monte Carlo  
572 simulation toolkit. *Phys Med.* 2015;31(8):861-874. doi:10.1016/j.ejmp.2015.10.087
- 573 9. Incerti S, Kyriakou I, Bernal MA, et al. Geant4-DNA example applications for track  
574 structure simulations in liquid water: A report from the Geant4-DNA Project. *Med Phys.*  
575 2018;45(8):e722-e739. doi:10.1002/mp.13048
- 576 10. Friedland W, Schmitt E, Kundrát P, et al. Comprehensive track-structure based evaluation  
577 of DNA damage by light ions from radiotherapy-relevant energies down to stopping. *Sci*  
578 *Rep.* 2017;7(March):45161. doi:10.1038/srep45161
- 579 11. Lampe N, Karamitros M, Breton V, et al. Mechanistic DNA damage simulations in Geant4-  
580 DNA Part 2: Electron and proton damage in a bacterial cell. *Phys Medica.* 2018;48(June  
581 2017):146-155. doi:10.1016/j.ejmp.2017.12.008
- 582 12. Sakata D, Lampe N, Karamitros M, et al. Evaluation of early radiation DNA damage in a  
583 fractal cell nucleus model using Geant4-DNA. *Phys Medica.* 2019;62(January):152-157.  
584 doi:10.1016/j.ejmp.2019.04.010
- 585 13. Meylan S, Incerti S, Karamitros M, et al. Simulation of early DNA damage after the  
586 irradiation of a fibroblast cell nucleus using Geant4-DNA. *Sci Rep.* 2017;7(1):1-15.  
587 doi:10.1038/s41598-017-11851-4

- 588 14. Tang N, Bueno M, Meylan S, et al. Influence of chromatin compaction on simulated early  
589 radiation-induced DNA damage using Geant4-DNA. *Med Phys.* 2019;46(3):1501-1511.  
590 doi:10.1002/mp.13405
- 591 15. Agostinelli S, Allison J, Amako K, et al. GEANT4 - A simulation toolkit. *Nucl Instruments*  
592 *Methods Phys Res Sect A Accel Spectrometers, Detect Assoc Equip.* 2003;506(3):250-303.  
593 doi:10.1016/S0168-9002(03)01368-8
- 594 16. Allison J, Amako K, Apostolakis J, et al. Geant4 developments and applications. *IEEE Trans*  
595 *Nucl Sci.* 2006;53(1):270-278. doi:10.1109/TNS.2006.869826
- 596 17. Allison J, Amako K, Apostolakis J, et al. Recent developments in GEANT4. *Nucl*  
597 *Instruments Methods Phys Res Sect A Accel Spectrometers, Detect Assoc Equip.*  
598 2016;835:186-225. doi:10.1016/j.nima.2016.06.125
- 599 18. Karamitros M, Mantero A, Incerti S, et al. Modeling Radiation Chemistry in the Geant4  
600 Toolkit. *Prog Nucl Sci Technol.* 2011;2:503-508.  
601 <http://www.aesj.or.jp/publication/pnst002/data/503-508.pdf>.
- 602 19. Karamitros M, Luan S, Bernal MA, et al. Diffusion-controlled reactions modeling in  
603 Geant4-DNA. *J Comput Phys.* 2014;274:841-882. doi:10.1016/j.jcp.2014.06.011
- 604 20. Shin W-G, Ramos-Mendez J, Faddegon B, et al. Evaluation of the influence of physical and  
605 chemical parameters on water radiolysis simulations under MeV electron irradiation  
606 using Geant4-DNA. *J Appl Phys.* 2019;126(11):114301. doi:10.1063/1.5107511
- 607 21. Schuemann J, McNamara AL, Ramos-Méndez J, et al. TOPAS-nBio: An Extension to the  
608 TOPAS Simulation Toolkit for Cellular and Sub-cellular Radiobiology. *Radiat Res.*  
609 2018;191(2):125. doi:10.1667/RR15226.1

- 610 22. Ramos-Méndez J, Burigo LN, Schulte R, Chuang C, Faddegon B. Fast calculation of  
611 nanodosimetric quantities in treatment planning of proton and ion therapy. *Phys Med*  
612 *Biol.* 2018;63(23):235015. doi:10.1088/1361-6560/aaeeee
- 613 23. Ivanchenko V, Apostolakis J, Bagulya a., et al. Recent Improvements in Geant4  
614 Electromagnetic Physics Models and Interfaces. *3th Monte Carlo Conf MC2010.*  
615 2011;2:898-903. <http://hal.in2p3.fr/in2p3-00658779>.
- 616 24. Clifford P, Green NJB, Oldfield MJ, Pilling MJ, Pimblott SM. Stochastic Models of Multi-  
617 species Kinetics in Radiation-induced Spurs. *J Chem Soc, Faraday Trans 1.* 1986;82:2673-  
618 2689. doi:10.1039/F19868202673
- 619 25. Green NJB, Pilling MJ, Clifford P. Stochastic Modeling of Fast Kinetics in a Radiation Track.  
620 *Society.* 1990;94(1):251-258. doi:10.1021/j100364a041
- 621 26. Pimblott SM, Pilling MJ, Green NJB. Stochastic models of spur kinetics in water. *Int J*  
622 *Radiat Appl Instrumentation Part.* 1991;37(3):377-388. doi:10.1016/1359-  
623 0197(91)90006-N
- 624 27. Tomita H, Kai M, Kusama T, Ito A. Monte Carlo simulation of physicochemical processes  
625 of liquid water radiolysis. *Radiat Environ Biophys.* 1997;36(2):105-116.  
626 doi:10.1007/s004110050061
- 627 28. Gervais B, Beuve M, Olivera GH, Galassi ME. Numerical simulation of multiple ionization  
628 and high LET effects in liquid water radiolysis. *Radiat Phys Chem.* 2006;75(4):493-513.  
629 doi:10.1016/j.radphyschem.2005.09.015
- 630 29. Tomita H, Kai M, Kusama T, Ito A. Monte Carlo simulation of DNA strand-break induction  
631 in supercoiled plasmid pBR322 DNA from indirect effects. *Radiat Environ Biophys.*

- 632 1998;36(4):235-241. doi:10.1007/s004110050077
- 633 30. Karamitros M, Brown J, Lampe N, et al. Implementing the Independent Reaction Time  
634 method in Geant4 for radiation chemistry simulations. 2020.
- 635 31. Sanguanmith S, Meesungnoen J, Muroya Y, Lin M, Katsumura Y, Jay-Gerin JP. On the spur  
636 lifetime and its temperature dependence in the low linear energy transfer radiolysis of  
637 water. *Phys Chem Chem Phys*. 2012;14(48):16731-16736. doi:10.1039/c2cp42826a
- 638 32. Sano H, Tachiya M. Partially diffusion-controlled recombination. *J Chem Phys*.  
639 1979;71(3):1276-1282. doi:10.1063/1.438427
- 640 33. Tachiya M. Theory of diffusion-controlled reactions: Formulation of the bulk reaction  
641 rate in terms of the pair probability. *Radiat Phys Chem*. 1983;21(1-2):167-175.  
642 doi:10.1016/0146-5724(83)90143-7
- 643 34. Agostinelli S, Allison J, Amako K, et al. Geant4—a simulation toolkit. *Nucl Instruments  
644 Methods Phys Res Sect A Accel Spectrometers, Detect Assoc Equip*. 2003;506(3):250-303.  
645 doi:10.1016/S0168-9002(03)01368-8
- 646 35. Karamitros M. Extension de l'outil Monte Carlo généraliste Geant4 pour la simulation de  
647 la radiolyse de l'eau dans le cadre du projet Geant4-DNA. 2013.  
648 [https://www.dropbox.com/s/r4grkm83uprchcd/These\\_MKaramitros.pdf%5Cnpapers3://](https://www.dropbox.com/s/r4grkm83uprchcd/These_MKaramitros.pdf%5Cnpapers3://publication/uuid/6BC42EC2-1ECD-47CB-84EC-DECE3E1B2CD3)  
649 [publication/uuid/6BC42EC2-1ECD-47CB-84EC-DECE3E1B2CD3](https://www.dropbox.com/s/r4grkm83uprchcd/These_MKaramitros.pdf%5Cnpapers3://publication/uuid/6BC42EC2-1ECD-47CB-84EC-DECE3E1B2CD3).
- 650 36. Goulet T, Jay-Gerin JP. On the reactions of hydrated electrons with OH. and H<sub>3</sub>O<sup>+</sup>.  
651 Analysis of photoionization experiments. *J Chem Phys*. 1992;96(7):5076-5087.  
652 doi:10.1063/1.462751
- 653 37. Lazarakis P, Incerti S, Ivanchenko V, et al. Investigation of track structure and condensed

654 history physics models for applications in radiation dosimetry on a micro and nano scale  
655 in Geant4. *Biomed Phys Eng Express*. 2018;4(2):024001. doi:10.1088/2057-1976/aaa6aa

656 38. Emfietzoglou D. Inelastic cross-sections for electron transport in liquid water: A  
657 comparison of dielectric models. *Radiat Phys Chem*. 2003;66(6):373-385.  
658 doi:10.1016/S0969-806X(02)00504-2

659 39. Rudd ME, Kim Y-K, Märk T, Schou J, Stolterfoht N, Toburen LH. ICRU Report 55. *J Int*  
660 *Comm Radiat Units Meas*. 1996;os28(2):NP-NP. doi:10.1093/jicru/os28.2.Report55

661 40. Shin WG, Bordage MC, Emfietzoglou D, et al. Development of a new Geant4-DNA  
662 electron elastic scattering model for liquid-phase water using the ELSEPA code. *J Appl*  
663 *Phys*. 2018;124(22). doi:10.1063/1.5047751

664 41. Bote D, Salvat F, Jablonski A, Powell CJ. The effect of inelastic absorption on the elastic  
665 scattering of electrons and positrons in amorphous solids. *J Electron Spectros Relat*  
666 *Phenomena*. 2009;175(1-3):41-54. doi:10.1016/j.elspec.2009.07.003

667 42. Michaud M, Wen A, Sanche L. Cross Sections for Low-Energy (1–100 eV) Electron Elastic  
668 and Inelastic Scattering in Amorphous Ice. *Radiat Res*. 2003;159(1):3-22.  
669 doi:10.1667/0033-7587(2003)159[0003:csflee]2.0.co;2

670 43. Meesungnoen J, Jay-Gerin J-P, Filali-Mouhim A, Mankhetkorn S. Low-Energy Electron  
671 Penetration Range in Liquid Water. *Radiat Res*. 2002;158(5):657-660. doi:10.1667/0033-  
672 7587(2002)158[0657:leepri]2.0.co;2

673 44. Peukert D, Incerti S, Kempson I, et al. Validation and investigation of reactive species  
674 yields of Geant4-DNA chemistry models. *Med Phys*. 2019;46(2):983-998.  
675 doi:10.1002/mp.13332



- 676 45. Kreipl MS, Friedland W, Paretzke HG. Time- and space-resolved Monte Carlo study of  
677 water radiolysis for photon, electron and ion irradiation. *Radiat Environ Biophys.*  
678 2009;48(1):11-20. doi:10.1007/s00411-008-0194-8
- 679 46. Ramos-Méndez J, Perl J, Schuemann J, McNamara A, Paganetti H, Faddegon B. Monte  
680 Carlo simulation of chemistry following radiolysis with TOPAS-nBio. *Phys Med Biol.*  
681 2018;63(10):105014. doi:10.1088/1361-6560/aac04c
- 682 47. Uehara S, Nikjoo H. Monte Carlo simulation of water radiolysis for low-energy charged  
683 particles. *J Radiat Res.* 2006;47(1):69-81. doi:10.1269/jrr.47.69
- 684 48. Pimblott SM, LaVerne JA. Stochastic Simulation of the Electron Radiolysis of Water and  
685 Aqueous Solutions. *J Phys Chem A.* 1997;101(33):5828-5838. doi:10.1021/jp970637d
- 686 49. Bartels DM, Cook AR, Mudaliar M, Jonah CD. Spur decay of the solvated electron in  
687 picosecond radiolysis measured with time-correlated absorption spectroscopy. *J Phys*  
688 *Chem A.* 2000;104(8):1686-1691. doi:10.1021/jp992723e
- 689 50. Muroya Y, Lin M, Wu G, et al. A re-evaluation of the initial yield of the hydrated electron  
690 in the picosecond time range. *Radiat Phys Chem.* 2005;72(2-3):169-172.  
691 doi:10.1016/j.radphyschem.2004.09.011
- 692 51. El Omar AK, Schmidhammer U, Jeunesse P, et al. Time-dependent radiolytic yield of OH•  
693 radical studied by picosecond pulse radiolysis. *J Phys Chem A.* 2011;115(44):12212-  
694 12216. doi:10.1021/jp208075v
- 695 52. Wang F, Schmidhammer U, Larbre JP, Zong Z, Marignier JL, Mostafavi M. Time-  
696 dependent yield of the hydrated electron and the hydroxyl radical in D2O: A picosecond  
697 pulse radiolysis study. *Phys Chem Chem Phys.* 2018;20(23):15671-15679.

- 698 doi:10.1039/c8cp02276c
- 699 53. Laverne JA. OH Radicals and Oxidizing Products in the Gamma Radiolysis of Water.  
700 *Source Radiat Res Radiat Res Gamma Radiolysis Water Radiat Res.* 2000;(153):53-196.  
701 <http://www.jstor.org/stable/3580071>. Accessed February 15, 2017.
- 702 54. Yoshida H, Bolch WE, Jacobson KB, Turner JE. Measurement of free ammonia produced  
703 by X irradiation of glycylglycine in aqueous solution. *Radiat Res.* 1990;121(3):257-261.  
704 doi:10.2307/3577774
- 705 55. LaVerne JA, Štefanić I, Pimblott SM. Hydrated Electron Yields in the Heavy Ion Radiolysis  
706 of Water. *J Phys Chem A.* 2005;109(42):9393-9401. doi:10.1021/jp0530303
- 707 56. Burns WG. Effect of Radiation Type in Water Radiolysis. *J Chem SOC Faraday Trans I.*  
708 1981;77:2803-2813.
- 709 57. Appleby A, Schwarz HA. Radical and molecular yields in water irradiated by .gamma.-rays  
710 and heavy ions. *J Phys Chem.* 1969;73(6):1937-1941. doi:10.1021/j100726a048
- 711 58. Anderson AR, Hart EJ. Molecular Product and Free Radical Yields in the Decomposition of  
712 Water by Protons, Deuterons, and Helium Ions. *Radiat Res.* 1961;14(6):689-704.  
713 doi:10.2307/3571010
- 714 59. Sauer MC, Schmidt KH, Hart EJ, Naleway CA, Jonah CD. LET dependence of transient  
715 yields in the pulse radiolysis of aqueous systems with deuterons and alpha particles.  
716 *Radiat Res.* 1977;70(1):91-106. doi:10.2307/3574734
- 717 60. Elliot A. et al. Temperature Dependence of g Values for H<sub>2</sub>O and D<sub>2</sub>O irradiated with Low  
718 Linear Energy Transfer Radiation. *J Chem Soc Faraday Trans.* 1993;89(8):1193-1197.  
719 doi:10.1039/FT9938901193

- 720 61. Pastina B, LaVerne JA. Hydrogen Peroxide Production in the Radiolysis of Water with  
721 Heavy Ions. *J Phys Chem A*. 1999;103(11):1592-1597. doi:10.1021/jp984433o
- 722 62. Wasselin-Trupin V, Baldacchino G, Bouffard S, Hickel B. Hydrogen peroxide yields in  
723 water radiolysis by high-energy ion beams at constant LET. *Radiat Phys Chem*.  
724 2002;65(1):53-61. doi:10.1016/S0969-806X(01)00682-X
- 725 63. Crumière F, Vandendorre J, Essehli R, Blain G, Barbet J, Fattahi M. LET effects on the  
726 hydrogen production induced by the radiolysis of pure water. *Radiat Phys Chem*.  
727 2013;82(1):74-79. doi:10.1016/j.radphyschem.2012.07.010
- 728 64. Al-Samra EH, Green NJB. On the approximation of independent pairs in diffusion kinetics:  
729 Correlation of distances in a three-body system. *Phys Chem Chem Phys*. 2018;20(4):2872-  
730 2879. doi:10.1039/c7cp06929d
- 731 65. Pimblott SM, Green NJB. Stochastic modeling of partially diffusion-controlled reactions in  
732 spur kinetics. *J Phys Chem*. 1992;96(23):9338-9348. doi:10.1021/j100202a052
- 733 66. Meesungnoen J, Jay-Gerin J-P. Effect of multiple ionization on the yield of H<sub>2</sub>O<sub>2</sub>  
734 produced in the radiolysis of aqueous 0.4 M H<sub>2</sub>SO<sub>4</sub> solutions by high-LET 12C<sup>6+</sup> and  
735 20Ne<sup>9+</sup> ions. *Radiat Res*. 2005;164(5):688-694. doi:10.1667/RR3459.1
- 736 67. Stroustrup B. *The C++ Programming.*; 1986.  
737